Supporting Information

Influence of the Iodide to Bromide Ratio on Crystallographic and Optoelectronic Properties of Rubidium Antimony Halide Perovskites

Stefan Weber[†], Thomas Rath[†], Kathrin Fellner[†], Roland Fischer[#], Roland Resel[§], Birgit Kunert[§], Theodoros Dimopoulos[‖], Andreas Steinegger[⊥], Gregor Trimmel[†]*

† Institute for Chemistry and Technology of Materials (ICTM), NAWI Graz, Graz University of Technology, Stremayrgasse 9, 8010 Graz, Austria

Institute of Inorganic Chemistry, NAWI Graz, Graz University of Technology, Stremayrgasse 9, 8010 Graz, Austria

§ Institute of Solid State Physics, NAWI Graz, Graz University of Technology, Petersgasse 16, 8010 Graz, Austria

‖ AIT Austrian Institute of Technology, Center for Energy, Photovoltaic Systems, Giefinggasse 4, 1210 Vienna, Austria

⊥ Institute of Analytical Chemistry and Food Chemistry, NAWI Graz, Graz University of Technology, Stremayrgasse 9, 8010 Graz, Austria

*Thomas Rath – thomas.rath@tugraz.at

Single Crystal X-ray structure analysis:

Suitable single crystals of compounds were immersed in silicone oil, mounted using a glass fiber and frozen in the cold nitrogen stream (100K). X-ray diffraction data were collected at low temperature on a Bruker Kappa APEX II diffractometer using Mo K_a radiation (λ = 0.71073 Å) generated by an INCOATEC micro-focus source.

The data reduction and absorption correction was performed with the Bruker SMART[1] and Bruker SADABS[2], respectively. The structures were solved with SHELXT[3] by direct methods and refined with SHELXL[4] by least-square minimization against F^2 using first isotropic and later anisotropic thermal parameters for all atoms. To assess the Br^-/I^- ratio in the mixed perovskites $Rb_3Sb_2Br_{9-x}I_x$, the halide positions in the crystals were treated as substitutional disorder in SHELXL (Part 1 for bromide and Part 2 for iodide ions) for which a second free variable was refined to give the Br^-/I^- ratio, while their sum accounts to 100% occupancy in total. Halide positions and anisotropic displacements parameters were therefore constrained pairwise to be identical using EADP and EXYZ commands as splitting over two positions remained unsuccessful.

The space group assignments and structural solutions were evaluated using PLATON.[5,6]

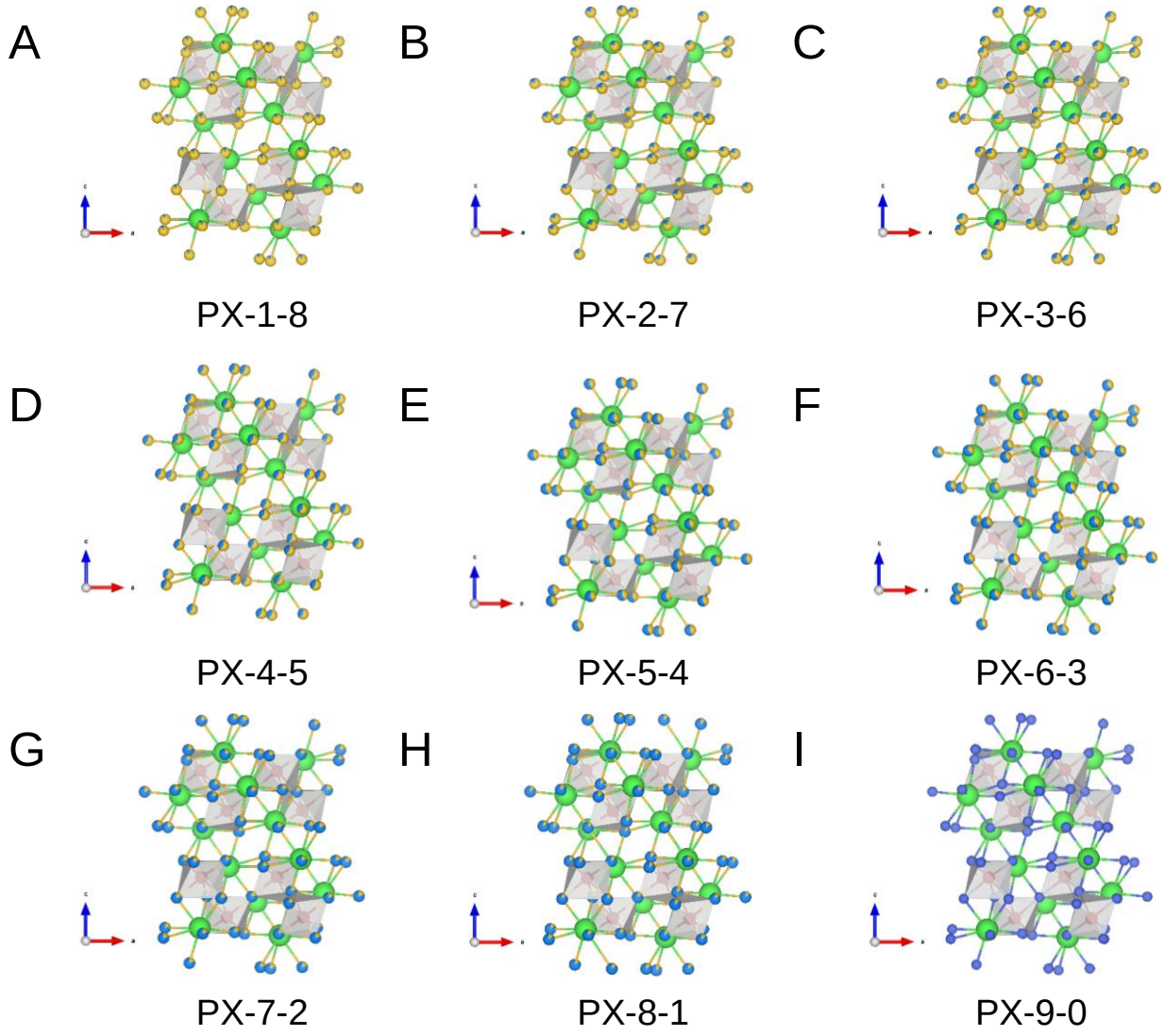

Figure S1. Crystal structures of the prepared $Rb_3Sb_2Br_{9-x}I_x$ samples obtained from single crystal X-ray diffraction: PX-1-8 (A), PX-2-7 (B), PX 3-6 (C), PX-4-5 (D), PX-5-4 (E), PX-6-3 (F), PX-7-2 (G), PX-8-1 (H), and PX-9-0 (I). Green: Rb, red: Sb, yellow: I, blue: Br. The crystal structure of the $Rb_3Sb_2I_9$ sample is shown in the main part of the manuscript.

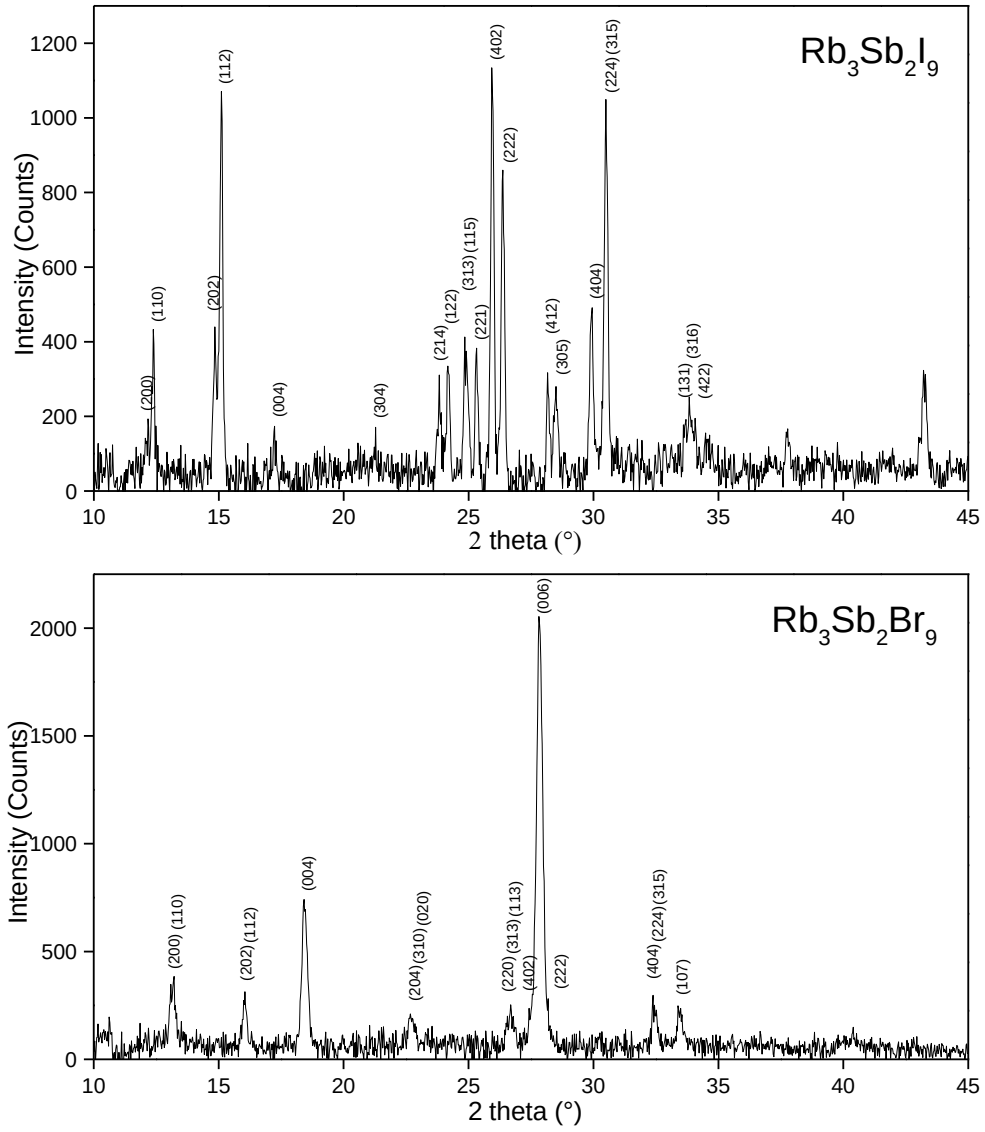

Figure S2. XRD patterns of $Rb_3Sb_2I_9$ and $Rb_3Sb_2Br_9$ thin films with assigned (hkl) values. The hkl values have been calculated via PowderCell 2.0 from the crystal structure data ($Rb_3Sb_2I_9$: ICSD 243727;[7] $Rb_3Sb_2Br_9$: ISCD 431322[8]) from the ICSD database.

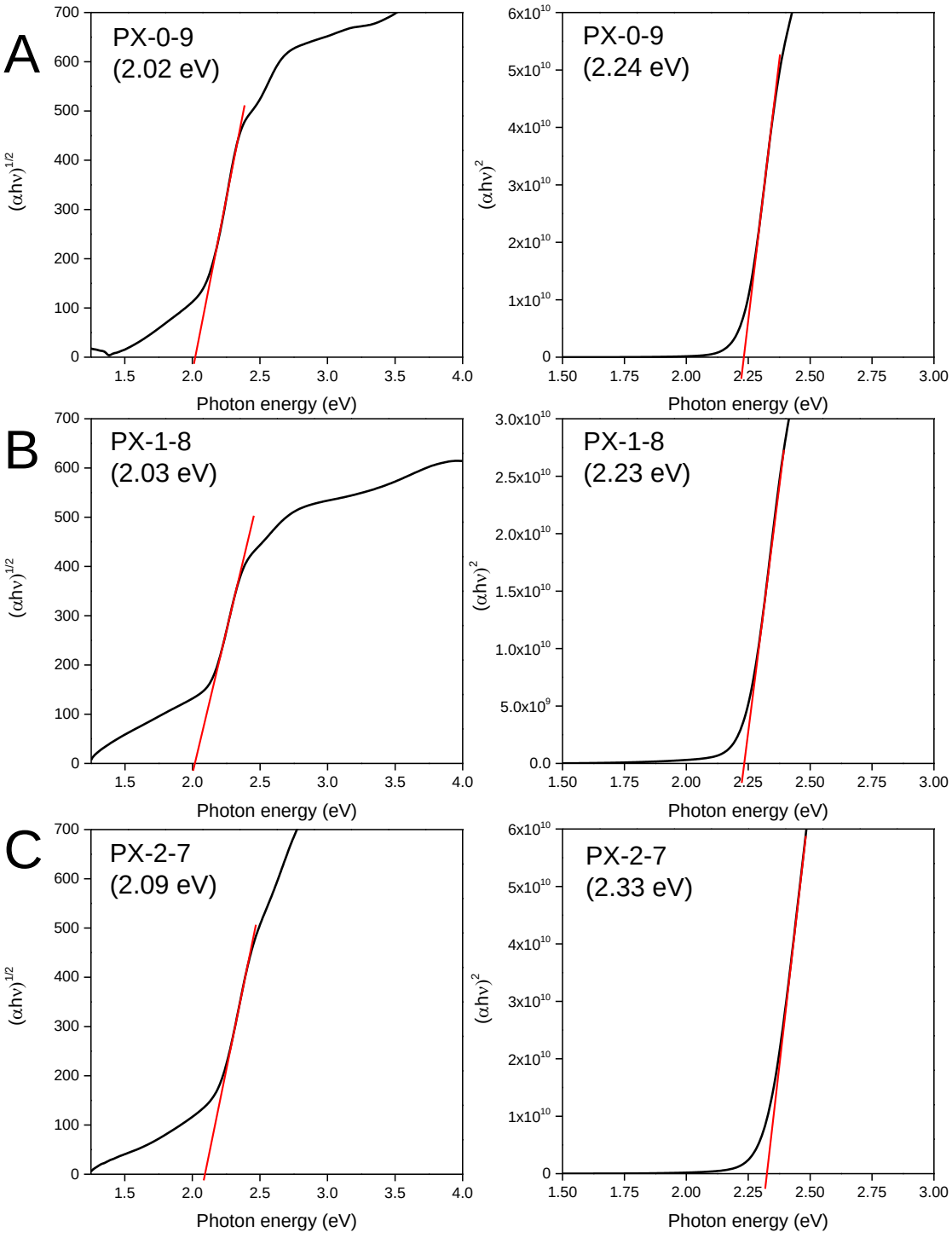
A
PX-0-9
(2.02 eV)
(αhν)^1/2
Photon energy (eV)
PX-0-9
(2.24 eV)
(αhν)^2
Photon energy (eV)
B
PX-1-8
(2.03 eV)
(αhν)^1/2
Photon energy (eV)
PX-1-8
(2.23 eV)
(αhν)^2
Photon energy (eV)
C
PX-2-7
(2.09 eV)
(αhν)^1/2
Photon energy (eV)
PX-2-7
(2.33 eV)
(αhν)^2
Photon energy (eV)

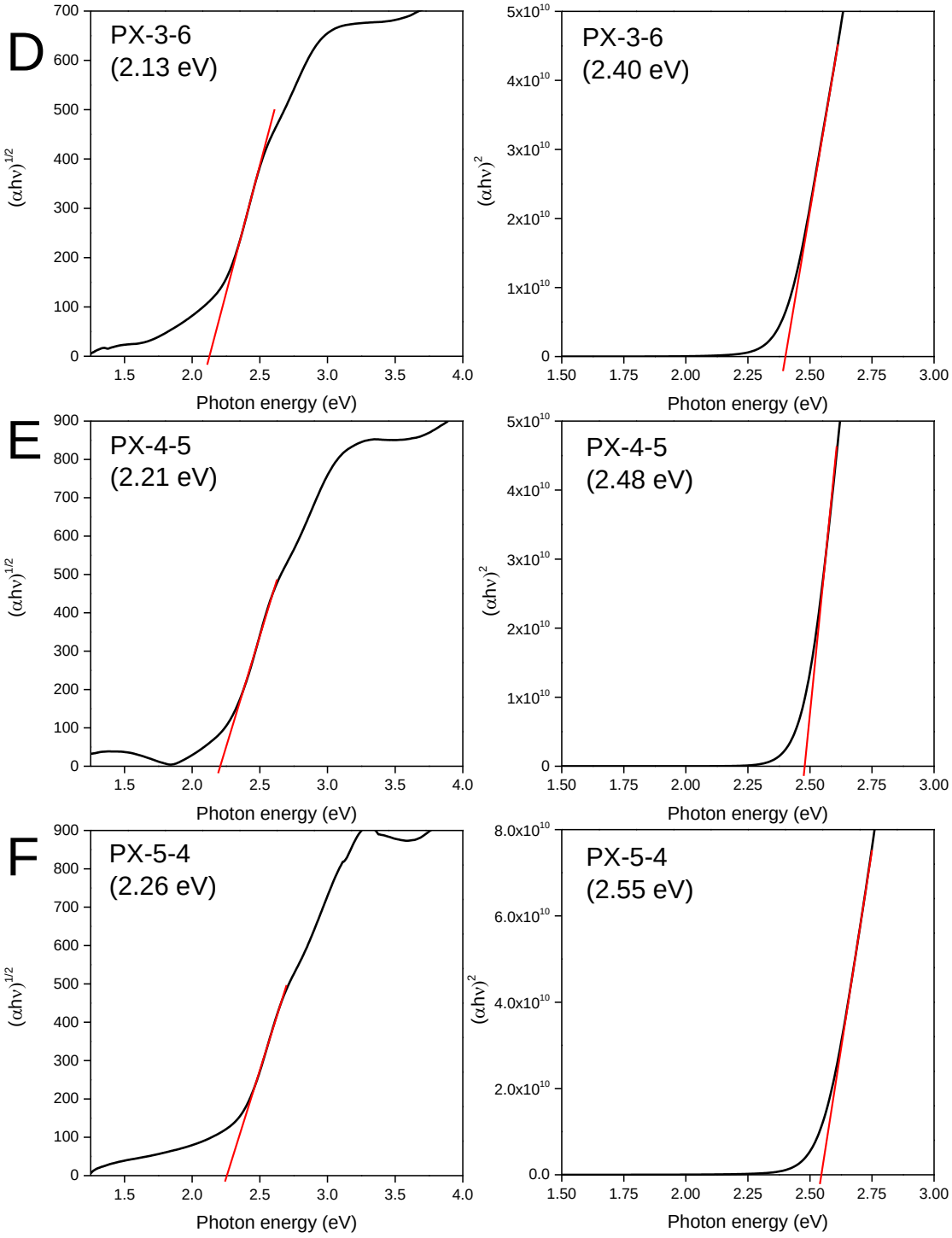
D
PX-3-6
(2.13 eV)
(αhν)^1/2
Photon energy (eV)
PX-3-6
(2.40 eV)
(αhν)^2
Photon energy (eV)
E
PX-4-5
(2.21 eV)
(αhν)^1/2
Photon energy (eV)
PX-4-5
(2.48 eV)
(αhν)^2
Photon energy (eV)
F
PX-5-4
(2.26 eV)
(αhν)^1/2
Photon energy (eV)
PX-5-4
(2.55 eV)
(αhν)^2
Photon energy (eV)

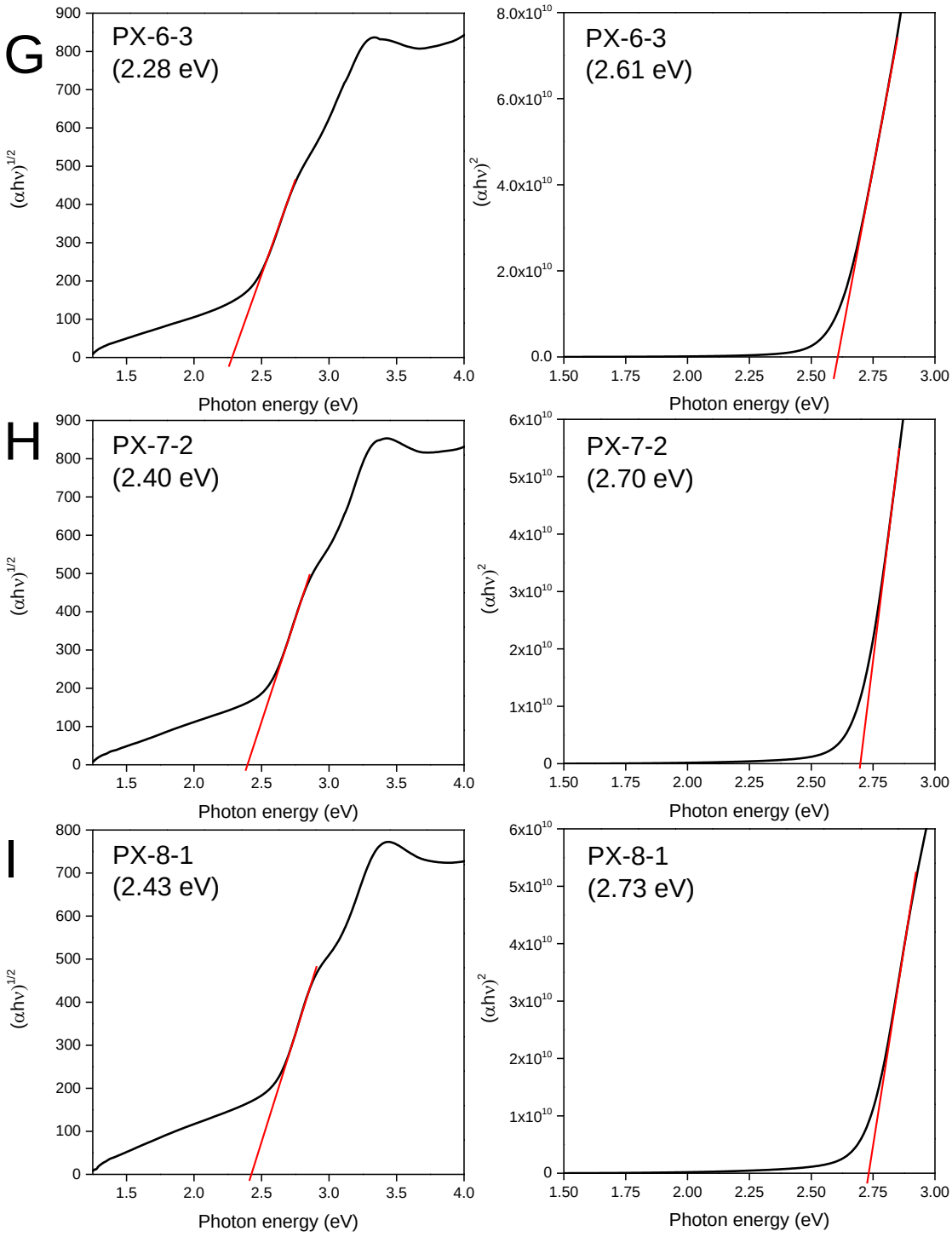
G
PX-6-3
(2.28 eV)
(αhν)^1/2
Photon energy (eV)
PX-6-3
(2.61 eV)
(αhν)^2
Photon energy (eV)
H
PX-7-2
(2.40 eV)
(αhν)^1/2
Photon energy (eV)
PX-7-2
(2.70 eV)
(αhν)^2
Photon energy (eV)
I
PX-8-1
(2.43 eV)
(αhν)^1/2
Photon energy (eV)
PX-8-1
(2.73 eV)
(αhν)^2
Photon energy (eV)

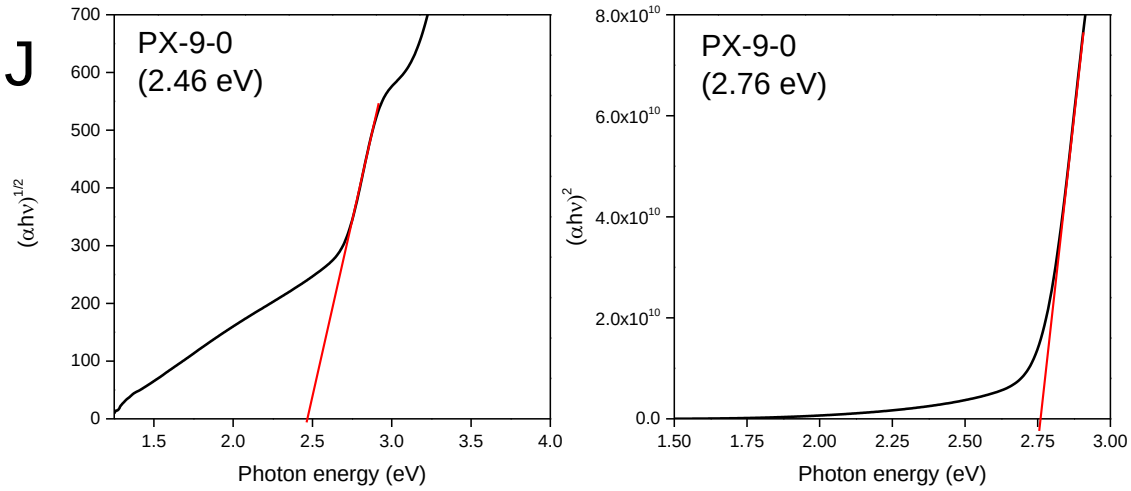

Figure S3. Tauc plots for indirect (left side) and direct (right side) allowed transitions and the corresponding band gaps of the following $Rb_3Sb_2Br_{9-x}I_x$ samples: PX-0-9 (A), PX-1-8 (B), PX-2--7 (C), PX-3-6 (D), PX-4-5 (E), PX-5-4 (F), PX-6-3 (G), PX-7-2 (H), PX-8-1 (I), PX-9-0 (J).

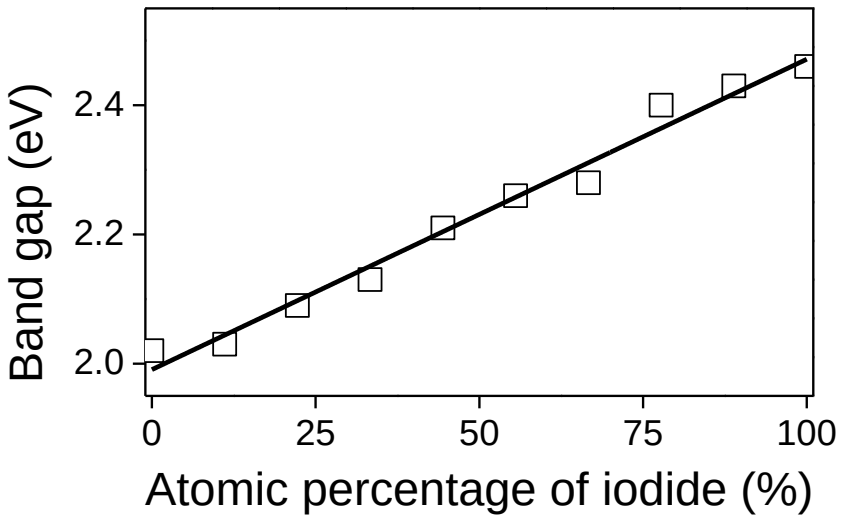

Figure S4. Correlation of the band gap of the $Rb_3Sb_2Br_{9-x}I_x$ samples with the atomic percentage of iodide. All samples showed an indirect band gap.

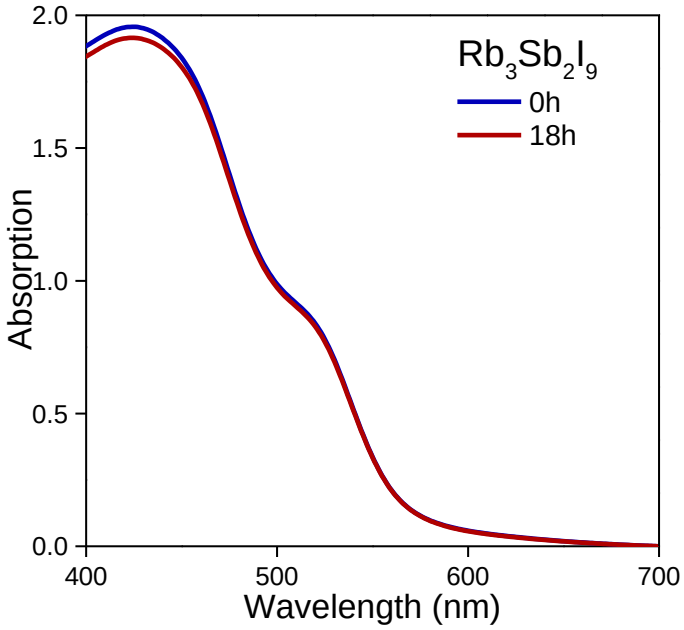

Figure S5. UV-Vis absorption spectra of a $Rb_3Sb_2I_9$ thin film before and after ageing for 18 h under ambient conditions.

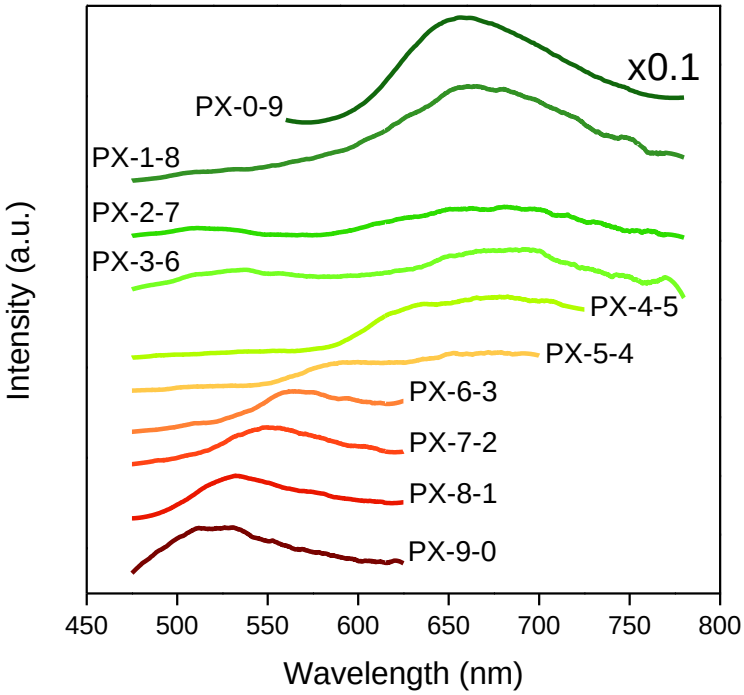

Figure S6. PL spectra of $Rb_3Sb_2Br_{9-x}I_x$ perovskite single crystals. The excitation wavelengths are given in Table S1.

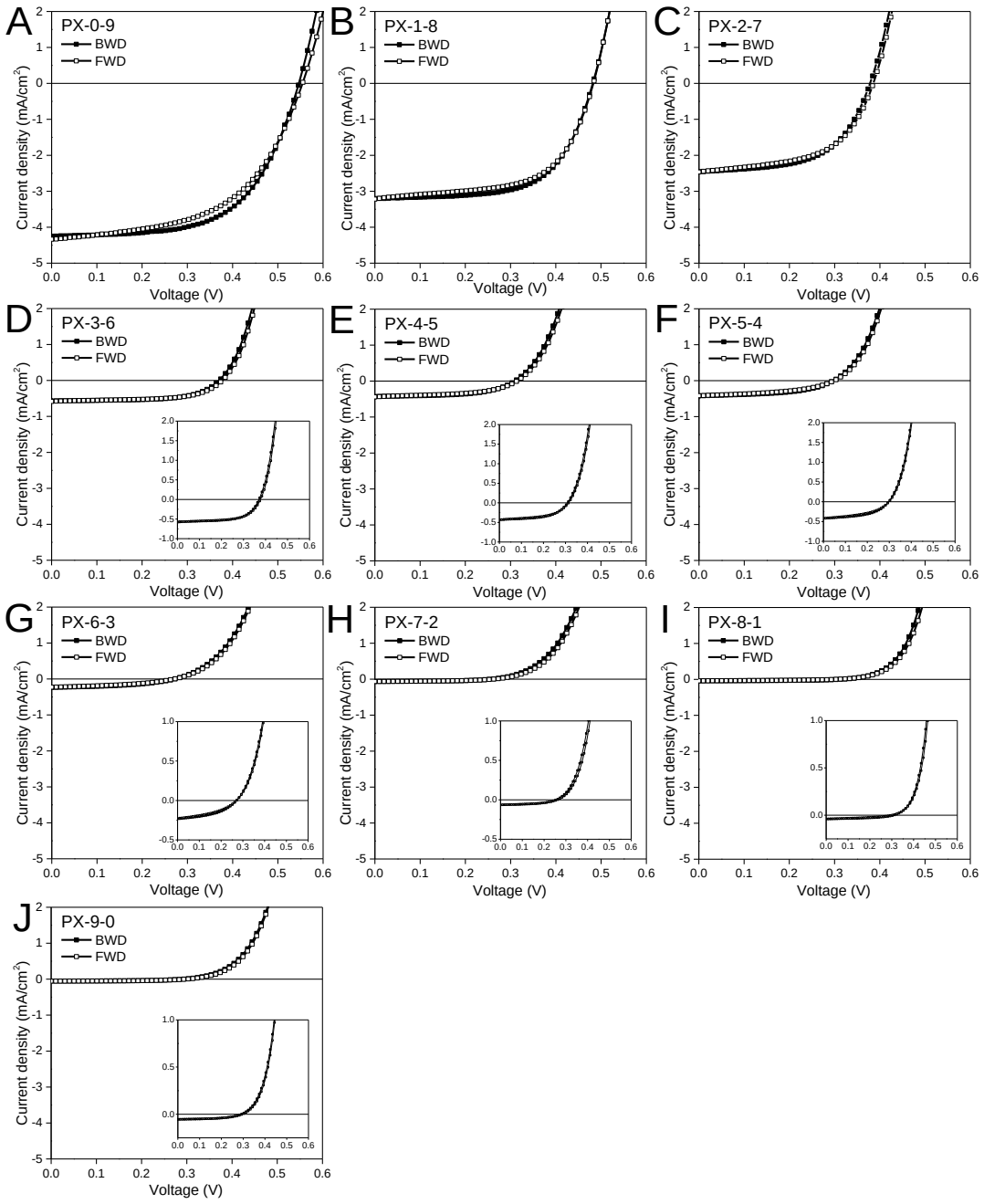

Figure S7. J-V curves of $Rb_3Sb_2I_{9-x}Br_x$ –based solar cells measured in forward (hollow symbols) and backward (solid symbols) scan direction (scan rate 100 mV/s). PX-0-9 (A), PX-1-8 (B), PX-2-7 (C), PX-3-6 (D), PX-4-5 (E), PX-5-4 (F), PX-6-3 (G), PX-7-2 (H), PX-8-1 (I), PX-9-0 (J).

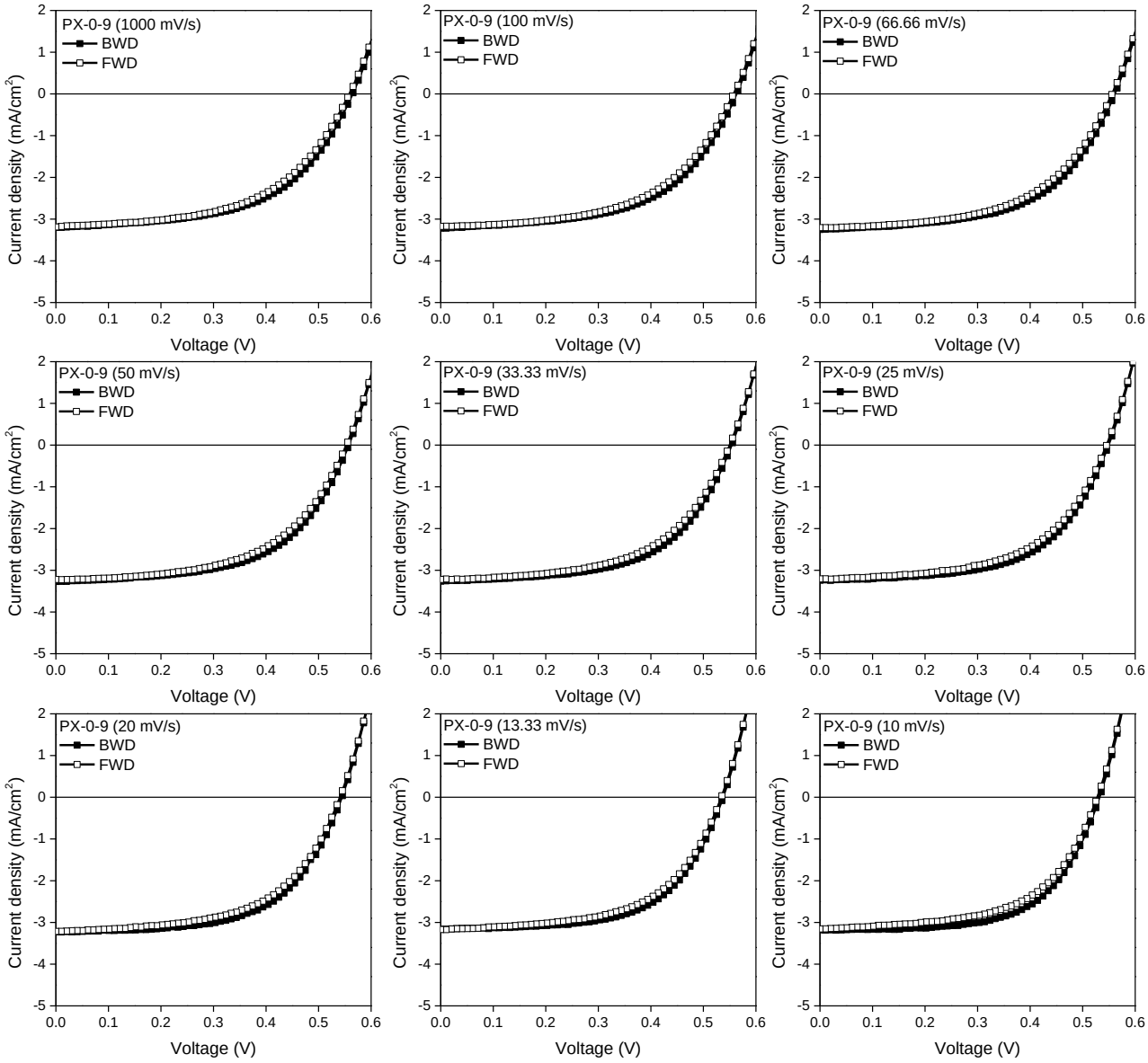

Figure S8. J-V curves of $Rb_3Sb_2I_9$ based solar cells measured in forward (hollow symbols) and backward (solid symbols) scan direction with different scan rates from 1000 mV/s to 10 mV/s. The corresponding characteristic parameters are given in Table S4.

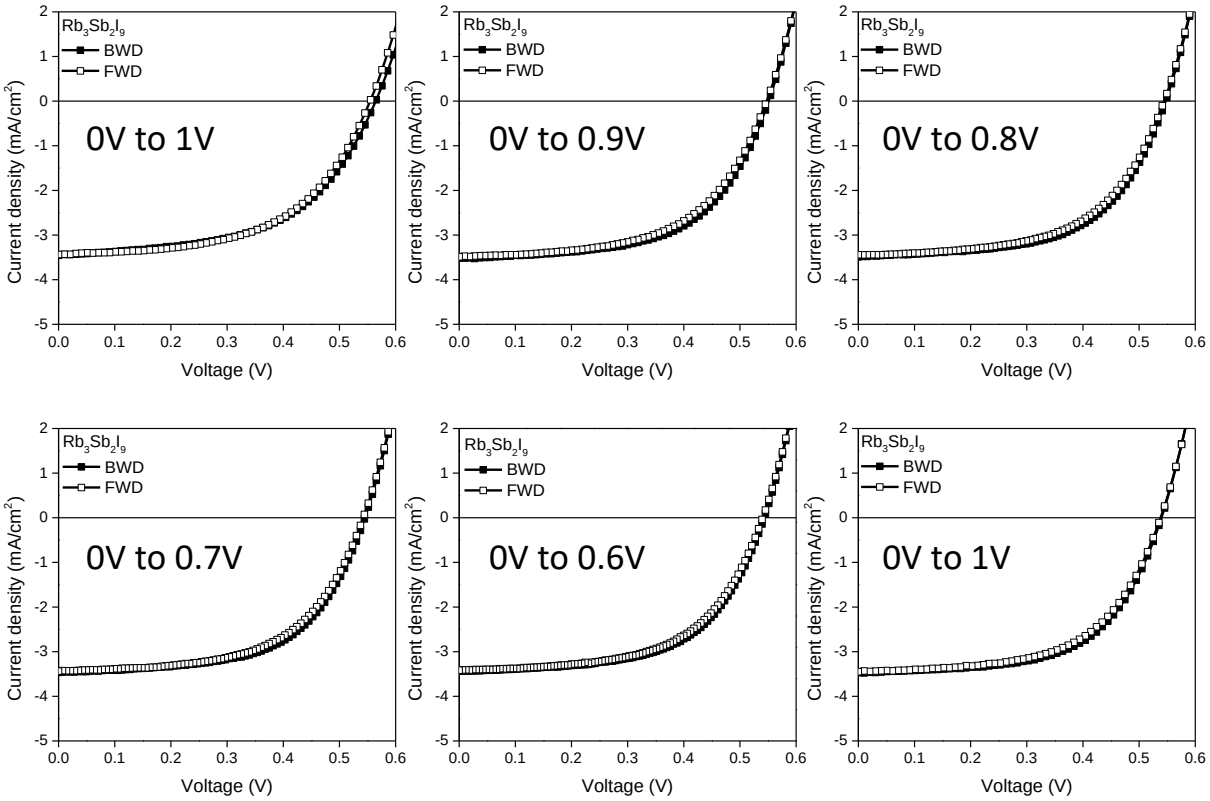

Figure S9. J-V curves of $Rb_3Sb_2I_9$ based solar cells measured in forward (hollow symbols) and backward (solid symbols) scan direction with different starting/end values. The corresponding characteristic parameters are summarized in Table S5.

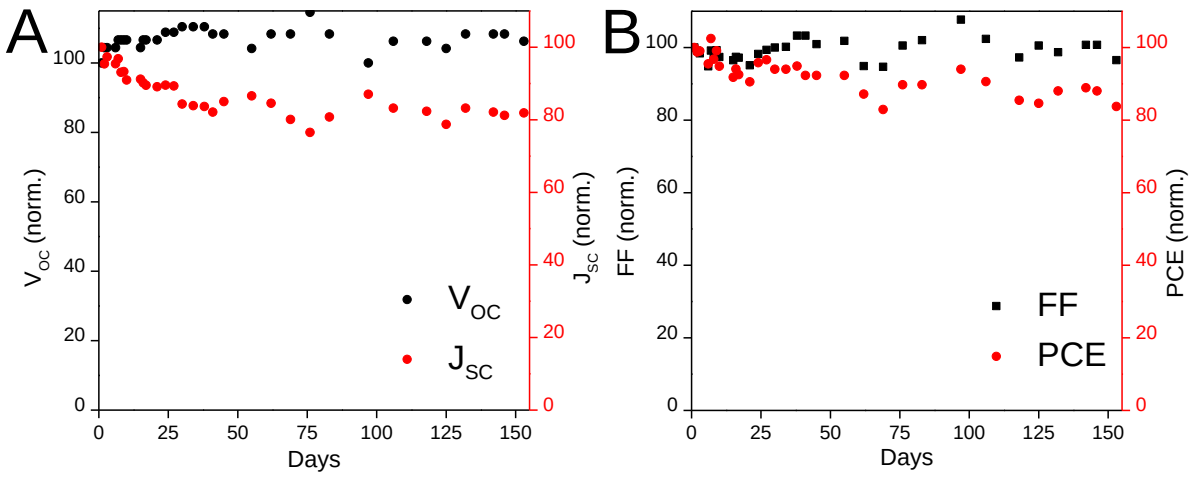

Figure S10. Stability data of a $Rb_3Sb_2I_9$ perovskite-based solar cell tested for more than 150 days (storage under inert conditions). The values were normalized with V_{OC} and J_{SC} shown in (A) and FF and PCE shown in (B).

Table S1. Excitation wavelengths used for the photoluminescence measurements of the $Rb_3Sb_2Br_{9-x}I_x$ perovskite films and single crystals

Sample	Excitation wavelength (nm) (Thin film)	Excitation wavelength (nm) (Single crystal)
PX-0-9	475	425
PX-1-8	475	425
PX-2-7	475	425
PX-3-6	425	425
PX-4-5	400	425
PX-5-4	425	425
PX-6-3	425	425
PX-7-2	425	425
PX-8-1	425	425
PX-9-0	425	425

Table S2. Characteristic parameters of the solar cells used for the measurements of the EQE spectra (measured with a 2.65x2.65 mm shadow mask)

	V_{OC} (V)	J_{SC} (mA/cm^2)	FF (%)	PCE (%)
PX-0-9	0.52	3.54	61.2	1.11
PX-1-8	0.45	2.76	64.6	0.81
PX-2-7	0.41	1.88	57.2	0.44
PX-3-6	0.39	0.43	60.7	0.11

Table S3. Characteristic parameters of $Rb_3Sb_2Br_{9-x}I_x$-based solar cells measured in backward (BWD) and forward (FWD) scan direction. The corresponding J-V curves are shown in Figure S6

		V_{OC} (V)	**J_{SC} (mA/cm^2)**	**FF (%)**	**PCE (%)**
PX-0-9	BWD	0.55	4.25	59.5	1.37
	FWD	0.56	4.33	53.1	1.27
PX-1-8	BWD	0.48	3.20	62.1	0.96
	FWD	0.48	3.22	59.5	0.92
PX-2-7	BWD	0.37	2.45	57.6	0.53
	FWD	0.38	2.46	54.9	0.52
PX-3-6	BWD	0.37	0.57	61.8	0.13
	FWD	0.37	0.58	60.2	0.13
PX-4-5	BWD	0.31	0.43	55.1	0.07
	FWD	0.31	0.44	51.2	0.07
PX-5-4	BWD	0.29	0.42	51.2	0.06
	FWD	0.30	0.42	45.0	0.06
PX-6-3	BWD	0.27	0.23	44.5	0.028
	FWD	0.27	0.23	40.5	0.025
PX-7-2	BWD	0.25	0.06	50.0	0.008
	FWD	0.26	0.07	45.2	0.008
PX-8-1	BWD	0.31	0.04	46.8	0.006
	FWD	0.30	0.04	37.0	0.005
PX-9-0	BWD	0.29	0.05	51.7	0.007
	FWD	0.29	0.06	50.5	0.008

Table S4: Characteristic parameters of a $Rb_3Sb_2I_9$-based solar cell measured in backward (BWD) and forward (FWD) scan direction whereas the scan rate was varied from 1000 mV/s to 10 mV/s. The corresponding J-V curves (BWD/FWD) are shown in Figure S8

Scan rate		**V_{OC} (V)**	**J_{SC} (mA/cm^2)**	**FF (%)**	**PCE (%)**
1000 mV/s	BWD	0.57	3.20	54.9	0.99
	FWD	0.56	3.19	53.6	0.95
100 mV/s	BWD	0.57	3.22	55.0	1.00
	FWD	0.56	3.17	54.1	0.96
66.66 mV/s	BWD	0.57	3.25	55.4	1.02
	FWD	0.56	3.21	54.4	0.97
50 mV/s	BWD	0.56	3.27	56.7	1.02
	FWD	0.56	3.22	54.8	0.97
33.33 mV/s	BWD	0.56	3.26	57.1	1.03
	FWD	0.55	3.22	55.9	0.98
25 mV/s	BWD	0.55	3.24	58.6	1.03
	FWD	0.55	3.21	56.0	0.97
20 mV/s	BWD	0.55	3.23	59.0	1.03
	FWD	0.55	3.21	55.9	0.97
13.33 mV/s	BWD	0.54	3.16	60.2	1.01
	FWD	0.54	3.17	56.9	0.96
10 mV/s	BWD	0.54	3.18	60.8	1.02
	FWD	0.53	3.16	57.7	0.96

Table S5: Characteristic parameters of a $Rb_3Sb_2I_9$-based solar cell measured in backward (BWD) and forward (FWD) scan direction whereas the starting voltage was varied from 1000 mV to 600 mV in 100 mV steps. The corresponding J-V curves (BWD/FWD) are shown in Figure S9

Starting voltage		**V_{OC} (V)**	**J_{SC} (mA/cm^2)**	**FF (%)**	**PCE (%)**
0 – 1000 mV	BWD	0.57	3.46	53.8	1.06
	FWD	0.56	3.44	54.6	1.05
0 – 900 mV	BWD	0.55	3.52	57.3	1.11
	FWD	0.55	3.49	56.6	1.07
0 – 800 mV	BWD	0.55	3.49	57.6	1.10
	FWD	0.54	3.44	57.2	1.06
0 – 700 mV	BWD	0.54	3.47	58.2	1.10
	FWD	0.54	3.44	56.9	1.06
0 – 600 mV	BWD	0.55	3.43	58.3	1.08
	FWD	0.54	3.42	57.3	1.05
0 – 1000 mV (02)	BWD	0.54	3.47	59.7	1.10
	FWD	0.54	3.45	58.1	1.06

References

[1] Bruker (**2007**). SMART. Bruker AXS Inc., Madison, Wisconsin, USA.

[2] Bruker (**2001**). SADABS. Bruker AXS Inc., Madison, Wisconsin, USA.

[3] Sheldrick, G. M. SHELXT - Integrated Space-Group and Crystal-Structure Determination. *Acta Crystallogr. Sect. A Found. Crystallogr*. **2015**, *71*, 3-8.

[4] Sheldrick, G. M. Crystal Structure Refinement with SHELXL. *Acta Crystallogr. Sect. C Struct. Chem.* **2015**, *71*, 3-8.

[5] Spek, A. L. Single-Crystal Structure Validation with the Program PLATON. *Journal of Applied Crystallography* **2003**, 36, 7-13.

[6] Spek, A. L. Structure Validation in Chemical Crystallography. *Acta Crystallographica Section D* **2009**, *65*, 148-155.

[7] McCall, K. M.; Stoumpos, C.; Kostina, S. S.; Kanatzidis, M. G.; Wessels, B. W. Strong Electron-Phonon Coupling and Self Trapped Excitons in the Defect Halide Perovskite $A_3M_2I_9$ (A = Cs, Rb; M = Bi, Sb). *Chem. Mater.* **2017**, *29*, 4129-4145.

[8] Chang, J.-H.; Doert, T.; Ruck, M. Structural Variety of Defect Perovskite Variants $M_3E_2X_9$ (M = Rb, Tl, E = Bi, Sb, X = Br, I). *Z. Anorg. Chem.* **2016**, *642*, 736-748.